Preprint Title	Plasmonic Nanosensor Based on Independently Tunable Multiple Fano Resonances
Authors	Lin Cheng, Zelong Wang, Xiaodong He and Pengfei Cao
Publication Date	22 Jul 2019
Article Type	Full Research Paper
ORCID® iDs	Lin Cheng - https://orcid.org/0000-0002-3818-2781

Plasmonic Nanosensor Based on Independently Tunable Multiple Fano Resonances

Lin Cheng*[1], Zelong Wang[1], Xiaodong He[1], Pengfei Cao[1]

Address: [1]Institute of Optoelectronics&Electromagnetic Information, Lanzhou University, Lanzhou 730000, China

Email: chenglin@lzu.edu.cn

* Corresponding author

Abstract

A novel refractive index nanosensor with compound structures is proposed in this paper. It consists of three different kinds of resonators and two stubs which are side-coupled to a metal-dielectric-metal (MDM) waveguide. By utilizing numerical investigation with the finite element method (FEM), the simulation results show that the transmission spectrum of the nanosensor has as much as five sharp peaks of Fano resonance. Due to their different resonance mechanisms, each peak of resonances can be independently tuned by adjusting the corresponding parameters of the structure. In addition, the sensitivity of the nanosensor is up to $1900nm/RIU$, and it also has an excellent performance with a high group refractive index of 18. For the sake of different functions to practical applications, a legitimate combination of various different components, such as T-shaped, ring, and split-ring cavities, has been proposed to make the na-

nosensor dramatically reduce its dimensions without sacrificing performance. These designing concepts pave a new way to construct such compact on-chip plasmonic structures, and it can be widely applied to nanosensors, optical splitters, filters, optical switches, nonlinear photonic and slow-light devices.

Keywords

Nanosensor; surface plasmon polaritons(SPPs); metal-dielectric-metal(MDM) waveguide; Fano resonance.

Introduction

Surface plasmon polaritons(SPPs) is a unique optical phenomenon which occurs in the coupling of electromagnetic waves with free electrons at the metal-dielectric interface[1]. It can overcome the classical diffraction limit of light. Based on this property, metal-dielectric-metal(MDM) waveguides have been designed and widely applied to manipulate light within sub-wavelength dimensions. And many plasmonic structures, such as high-sensitivity refractive index sensor[2], enhanced biochemical sensors[3], switches, filters[4], have been designed based on Fano resonance by utilizing MDM waveguide[3,5,6]. Due to the interference of continuous(bright) modes and discrete(dark) modes, Fano resonance exhibits the sharp asymmetric line shape characteristic[7], which has attracted more and more attention. The common design methods of these structures can be generally divided into three categories — First is that the input and output waveguides are direct coupled to both ends of the resonator[3,8-10], second is that the resonators are side coupled to one waveguide between the input and output ports[11-15], and third is that the input waveguide, output

waveguide and resonators are all coupled through a gap[2,16,17]. The common resonators are rectangular[6], ring[14], triangular[9], disk[18,19], hexagonal[20] and other special shapes. In recent years, many structures have been proposed to obtain the Fano resonance effect[20,21]. Obviously, a structure with only one resonant mode is hardly to have satisfactory effect in practical applications[20,22]. Therefore, the structures which can excited multimode resonances are proposed[23]. So far as is known, increasing the number of transmission peaks can effectively improve the accuracy and the fault tolerance of the structure. Independently adjusting the position of the resonance peaks can make the structure have a high suitability to different application, and the compact size is always desirable in the design of on-chip plasmonic structures. However, multiple resonance peaks generally mean more complex structure with hardly to obtain a highly independent tunability[24]. It is also a technical challenge to reduce the size of the structure under the premise of guaranteeing the performance[15].

In this paper, we proposed a compact plasmonic nanosensor which is composed of one MDM waveguide, two side-coupled stubs, and three gap-coupled resonators of a T-shaped, a ring and a split-ring separately. The transmission features of the structure are numerically simulated by finite element method (FEM). The simulation results show that the transmission spectrum has multiple Fano resonances. Moreover, each peak of Fano resonances can be independently and precisely tuned by changing the corresponding resonator's parameters. The characteristics of each resonance mode are further investigated in details. By comparing these resonators to each other, it can be found that the

resonator directly coupled to the MDM waveguide has a higher transmission, the asymmetric T-shaped resonator can generate multiple resonant modes, the ring resonator can produce a sharper transmission peak, and the split-ring resonator has the minimum size with more adjustable parameters under the premise of guaranteeing the performance. Hence, our compound structure combines the advantages of the various resonators, such as the asymmetric T-shaped, ring and split-ring, to obtain multiple Fano resonance modes with highly compact dimensions and independent tuning of peak position. Subsequently, the research on properties of refractive index nanosensor shows the maximum value of the sensitivity is $1900nm/RIU$ and the figure of merit (FOM) is 1199. Meanwhile, the group refractive index of the structure is up to 18. All these capabilities are excellent compared to similar reported nanosensors. Thus, our structure is potential for on-chip detection with high performance. Moreover, our study on the characteristics of different types of resonators also provides a powerful theoretical guidance for all-optical integration systems and ultra-compact plasmonic devices.

Theory and Model

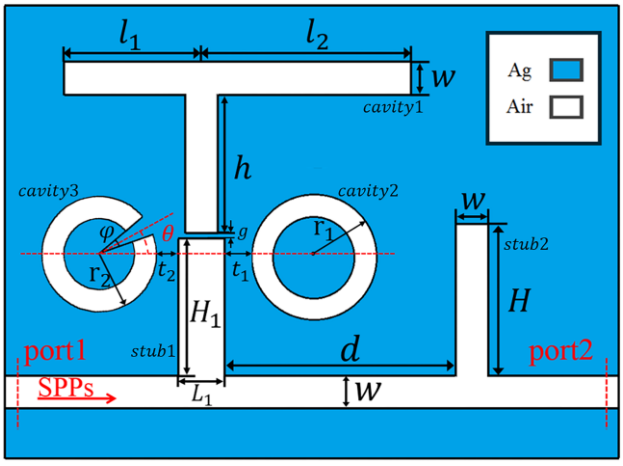

Figure. 1 Schematic diagram of the plasmonic nanosensor. Geometric parameters are labelled on the structure for the following discussion.

Figure. 1 shows the scheme diagram of our plasmonic nanosensor. It is composed of three resonators(an asymmetric T-shaped, a ring and a split-ring, respectively) which are gap-coupled to a bus waveguide with two stubs. For convenience, firstly we named the T-shaped resonator, the ring, the split-ring, the left stub and the right stub as $cavity1$, $cavity2$, $cavity3$, $stub1$ and $stub2$, respectively. The width of the bus waveguide, three cavities and $stub2$ are fixed at $w = 50nm$ in this paper. h is the height of the vertical part of $cavity1$ and its horizontal length is divided into l_1 and l_2. r_1 and r_2 are the outer radius of $cavity2$ and $cavity3$. The opening angle of $cavity3$ which is denoted by φ (here, $\varphi = 20°$). The angle between the centre line of the opening and the horizontal axis(the red-dash line as shown in Figure1) is marked as θ. L_1 and H_1 is the length and the height of $stub1$, H_2 is the height of $stub2$, and d is the distance between $stub1$ and $stub2$. The coupling distance between $stub1$ and $cavity1$ is represented by g, similarly t_1 and t_2 are the coupling distance from $cavity2$ and $cavity3$ to $stub1$, respectively. Given that the centre of the $cavity2$ and $cavity3$ has the same distance to the bus waveguide which is $215nm$. In the schematic diagram, the white and blue areas represent dielectric and metal respectively. The dielectric in the waveguide and cavities is air, of which the relative permittivity is $\varepsilon_d = 1$. The metal is silver, with permittivity ε_m characterized by the Drude model covering the wavelength range of 1000~2000nm of interest[25].

$$\varepsilon_m(\omega) = \varepsilon_\infty - \omega_p/(\omega^2 + i\omega\gamma_p) \quad (1)$$

where $\varepsilon_\infty = 3.7$ is the electric constant at the infinite angular frequency, the bulk plasma frequency $\omega_p = 1.38 \times 10^{16} rad/s$, ω stands for the angle frequency of incident wave, the damping rate $\gamma_p = 2.73 \times 10^{13} rad/s$ characters the absorption loss. TM-polarized plane wave is launched from $port1$ to excite the SPPs. Here P_{in} and P_{out} stand for input and output power flows of the input $port1$ and output $port2$, respectively. The transmittance is defined as $T = P_{out}/P_{in}$.

Since the width of the bus waveguide is much smaller than the wavelength of the incident light, only a single propagation mode TM_0 can exist in the structure, of which the dispersion relation is determined by the following equation

$$\varepsilon_m \sqrt{\beta_{spp}^2 - \varepsilon_d k_0^2}\, tanh\left(\frac{w\sqrt{\beta_{spp}^2 - \varepsilon_d k_0^2}}{2}\right)$$

$$+\varepsilon_d \sqrt{\beta_{spp}^2 - \varepsilon_m k_0^2} = 0 \qquad (2)$$

where $\beta_{spp} = k_0 n_{eff}$ is the propagation constant of the SPPs in the waveguide, n_{eff} is the effective refractive index, $k_0 = 2\pi/\lambda$ is free space wavenumbers. Then the resonance wavelength of different modes for stub and resonators can be derived from the standing wave theory by the resonance condition as follows

$$\lambda_{stub} = \frac{4 n_{eff} L_{eff}}{(2m-1) - \varphi_r/\pi}, m = 1,2,3\ldots, \qquad (3)$$

and

$$\lambda_{res} = \frac{2 n_{eff} L_{eff}}{m - \varphi_r/\pi}, m = 1,2,3\ldots, \qquad (4)$$

where L_{eff} is the effective length of the cavity, and φ_r is the phase shift of SPPs reflected on the facets of the cavity.

The transmission characteristics of the plasmonic waveguide system can be analyzed by coupled mode theory(CMT). In this theory, the total field can be obtained by the superposition of various modes. When multiple modes are coupled in a narrow wavelength range, the phase difference of different modes cannot be ignored. Therefore, multimode interference coupled mode theory(MICMT) is proposed on the basis of CMT by adding phase difference effect, and its equations are expressed as follows

$$\frac{da_n}{dt} = j\omega_n a_n - \left(\frac{1}{\tau_{n0}} + \frac{1}{\tau_{n1}} + \frac{1}{\tau_{n2}}\right) a_n$$

$$+\kappa_{n1} S_{1+} + \kappa_{n2} S_{2+} \qquad (5)$$

$$S_{1-} = -S_{1+} + \sum_n \kappa_{n1}^* \, a_n e^{j\varphi_{n1}} \qquad (6)$$

$$S_{2-} = -S_{2+} + \sum_n \kappa_{n2}^* \, a_n e^{j\varphi_{n2}} \qquad (7)$$

Where a_n and ω_n are the field amplitude and resonant frequency of the nth mode, respectively. τ_{n0} is the decay time of internal loss of the nth mode in resonant system. τ_{n1}, τ_{n2} are the decay time of the coupling between the resonant system and left, right part of the bus waveguide, respectively. κ_{n1} and κ_{n2} are the coefficient expressing the degree of the coupling between the resonant system and the waveguide. φ_{n1} and φ_{n2} are the complex amplitude phases of the nth resonant mode coupled to the waveguides. $S_{i\pm}$ are the field amplitudes in each part of the waveguide($i = 1, 2$) for outgoing($-$) or incoming($+$) from the resonator. In this paper, only $port1$ has TM wave incidence. The input and output port are symmetrical with the same w about the resonance system. Hence, $S_{2+} = 0$, $\tau_{n1} = \tau_{n2} = \tau_n$, and the transmittance T is satisfied the following equation

$$T = |t|^2 = |\frac{S_{2-}}{S_{1+}}|^2$$

$$= |\sum_n \frac{2e^{j\varphi_n}}{-j(\omega-\omega_n)\tau_n+2+\frac{\tau_n}{\tau_{n0}}}|^2 \qquad (8)$$

Where t is the transmission coefficient and φ_n is the total coupling phase difference of the nth resonant mode.

Results and Discussion

In this paper, the compound structure of our plasmonic nanosensor, as shown in Figure 1, is numerically investigated on finite element method(FEM), which is also comparative to MICMT. The transmittances are calculated according to the definition with Equation 8. It is well known that the excitation of Fano resonance requires the interaction of continuous (bright) modes and discrete (dark) modes. In our design, $stub1$ can afford to form the bright mode, and each of the three resonators ($cavity1$, $cavity2$, $cavity3$) can generate the different dark modes. To further reveal the resonance properties, like assembling as building blocks, we performed a series of numerical simulations to discuss the mechanism of our design.

Firstly, a simple layout consisting of the bus waveguide with $stub1$, was studied and the transmittance spectrum is depicted with blue dashed-line as shown in Figure 2a. When added $stub2$ into the beginning simple layout, one resonance peak is excited as shown in red solid line in Figure 2a. The height of $stub2(H)$ and the distance between two stubs(d) are set to $500nm$ and $750nm$, respectively. Obviously, the blue dashed line shows a wide dip around $1320nm$, which provides the bright mode. While the dark mode is excited by $stub1$, $stub2$ and

the middle part of bus waveguide between these two stubs, interacting with each other to get the first peak at 1066nm, denoted as $peak1$.

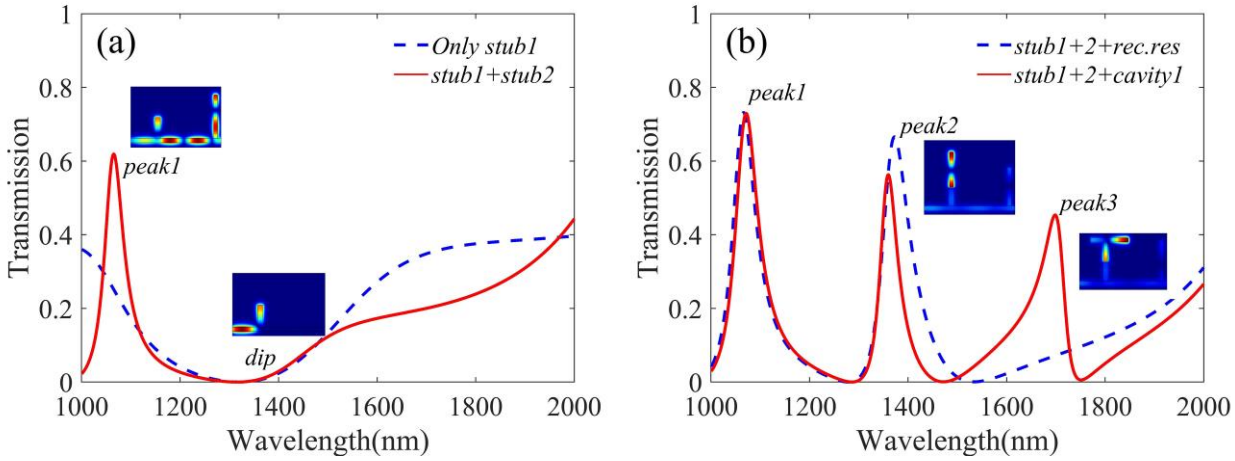

Figure 2 Transmission spectra of (a) only $stub1$(blue dashed line), $stub1$ and $stub2$(red solid line) side-inserted into bus waveguide, (b) two stubs and rectangular resonator(blue dashed line), two stubs and $cavity1$(red solid line) in the structure.

Based on the single mode system, a dual resonance mode system is constructed by side-coupling a rectangular resonator above $stub1$. The width and height of the rectangular resonator are $50nm$ and $450nm$ and the coupling distance g is $8nm$. The transmittance spectrum is shown in Figure 2b in blue dashed line, the second peak appeared at $1373nm$, labelled as $peak2$. In order to shrink the geometry and spare the level space, we replaced the rectangular resonator with an asymmetric T-shaped resonator named $cavity1$. The transmittance curve is plotted in Figure 2b with red solid line. The size parameters of $cavity1$ are $l_1 = 210nm$, $l_2 = 320nm$ and $h = 240nm$, respectively. Because of the asymmetry of T-shaped resonator $(l_1 \neq l_2)$, there is a third resonance peak emerged at

$1699nm$, denoted as $peak3$. The effective length l_{eff} of $cavity1$ are $l_1 + h = 450nm$ and $l_2 + h = 560nm$ corresponding to $peak2$ and $peak3$, respectively. The effective length l_{eff} in the rectangular resonator and $cavity1$ are the same, but in Fig2.b we can see $peak2$ has a slight shift on wavelength, this is because the n_{eff} of $cavity1$ is slightly larger than the rectangular resonator, therefore a slight blue shift is occurred when $cavity1$ is substituted to the rectangular resonator. All these theoretical analyses are consistent well with the aforementioned Equations (2-4).

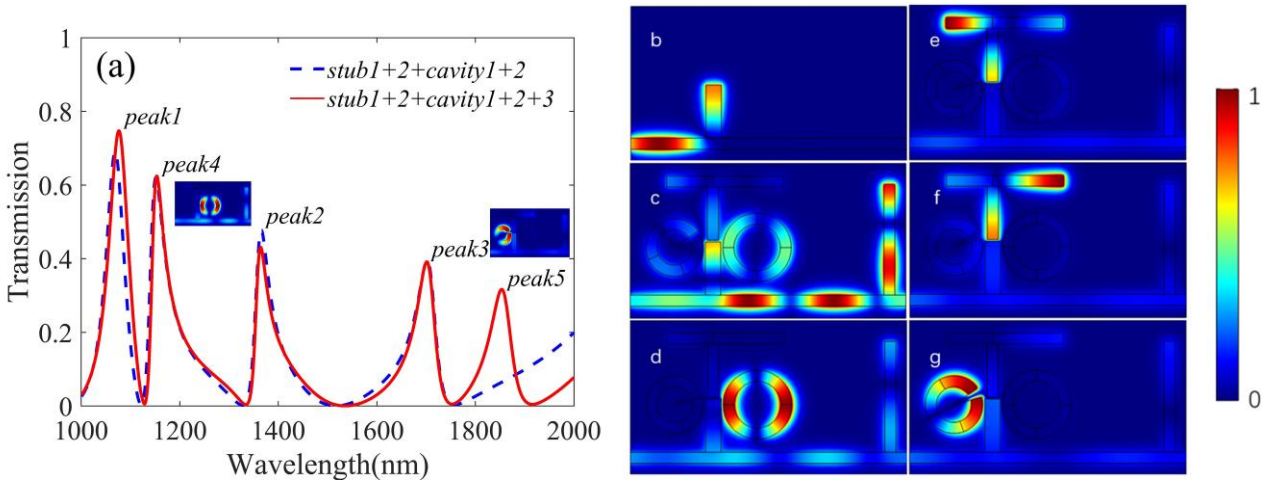

Figure 3 Transmission spectra of the structure with(red solid line) and without(blue dashed line) $cavity3$, (b) the distribution of normalized magnetic field $|H_z|$ at $1320nm$ with only $stub1$ inserted into bus waveguide. $|H_z|$ distribution of total compound structure at the resonance wavelengths of (c) $1077nm$, (d) $1364nm$, (e) $1702nm$, (f) $1154nm$, (g) $1854nm$.

By coupling a ring resonator, which is named $cavity2$ with a $155nm$ outer radius and $10nm$ coupling distance from the right side of $stub1$, a new resonance mode is induced near $peak1$, denoted as $peak4$. Also a new dip at $1122nm$ be-

tween $peak1(1069nm)$ and $peak4$ $(1152nm)$ appears, as shown in Figure 3a in blue dashed line. It attributes to the phase-coupling and the interference between the bright mode and various dark modes in a narrow wavelength range. Such dramatically changes from dip to peak can significantly improves the detection accuracy of the nanosensor.

Finally, a split-ring resonator named $cavity3$ is inserted into the left side of $stub1$. The relevant parameters of $cavity3$ are $r_2 = 130nm$, $\varphi = 20°$, $\theta = 25°$ and $t_2 = 9nm$. The corresponding transmission spectrum is shown in Figure 3a in red solid line, emerging a new Fano resonance peak at $1854nm$, denoted as $peak5$ due to the inserted $cavity3$.There is aslight deviation, which is mainly because the interference of adjacent modes and the neglect of the wavelength dependence of φ_r[26,27].

Moreover, Figure 3b shows the $|H_z|$ field of the structure only composed of $stub1$ and bus waveguide at $\lambda = 1320nm$. According to Equation 2 and 3, the incident and reflected waves in $stub1$ and the left part waveguide form constructive interference, while in the right part is destructive interference. Hence, the transmittance is almost 0, which is agree well with the situation of the dip inset in Figure 2a. Figure 3c-g corresponds to $peak1, 2, 3, 4$ and 5, respectively. Figure 3c illustrates that the magnetic field energy of $peak1$ at $1077nm$, which is mainly concentrated on $stub1$, $stub2$ and the middle part of bus waveguide between these two stubs. The $|H_z|$ of $peak2$ at $1364nm$ is shown in Figure 3d, almost all energy is limited in the left and bottom parts of $cavity1$. The similar situations for $peak3$, 4 and 5 are shown in Figure 3e, f and g, respectively. Obviously, each transmittance peak corresponds to a specific resonance element,

which provides a flexibility to design plasmonic devices on purpose with multiple Fano resonances.

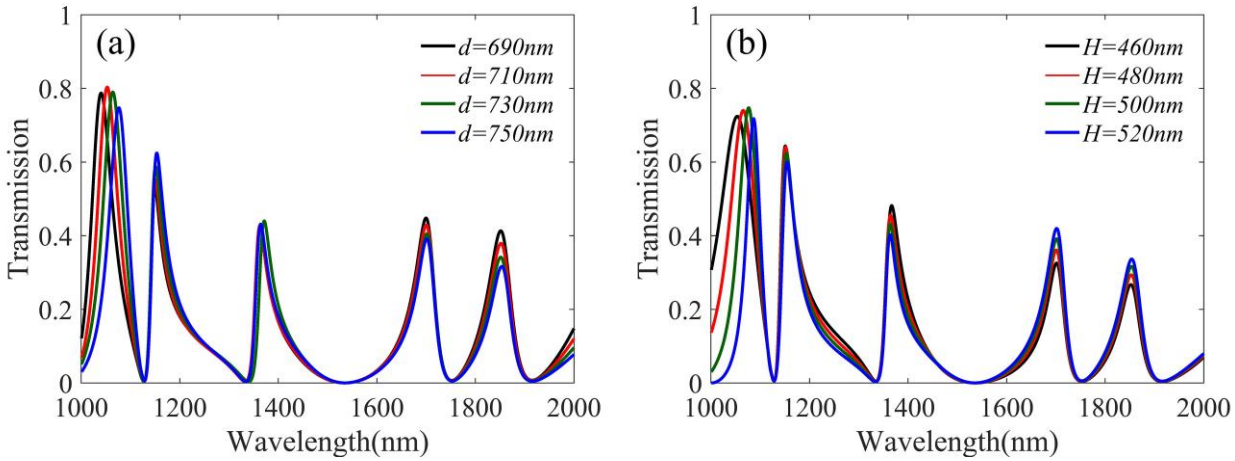

Figure 4 Dependence of the transmission on two parameters, (a) the distance d between two stubs and (b) the height H of $stub2$.

In the following part, we further investigated the parametric responses of each resonance element and discussed the performance of the nanosensor. For the sake of concise describe, each time only one parameter has a variation, the other parameters are constant. Figure 4a shows the transmission spectra of changing the distance d between two stubs. It was found that the resonance wavelength of $peak1$ will produce a significant red shift by increasing d, while the other four peaks almost remain unchanged. Figure 4b shows the resonance wavelength of $peak1$ also has a red shift by increasing the height H of $stub2$. It can be seen by comparing the Figure 4a and b that the changes of the full width at half maxima(FWHM) of $peak1$ is more stable when the parameter d is adjusted. This is mainly because the change of H has a larger influence on the symmetry of the resonance system than the change of d. Moreover, the transmittance of $peak1$ is higher than the others, due to the direct coupling between

the stubs and the waveguide. And it is worth mentioning that the continuous bright mode is only excited by $stub1$, while the discrete dark mode can be excited by either of the three cavities. Thus, $stub1$ plays the important role to excited both the bright mode and the dark mode in this resonance system. Similar structural design can significantly reduce device size in some specific situations.

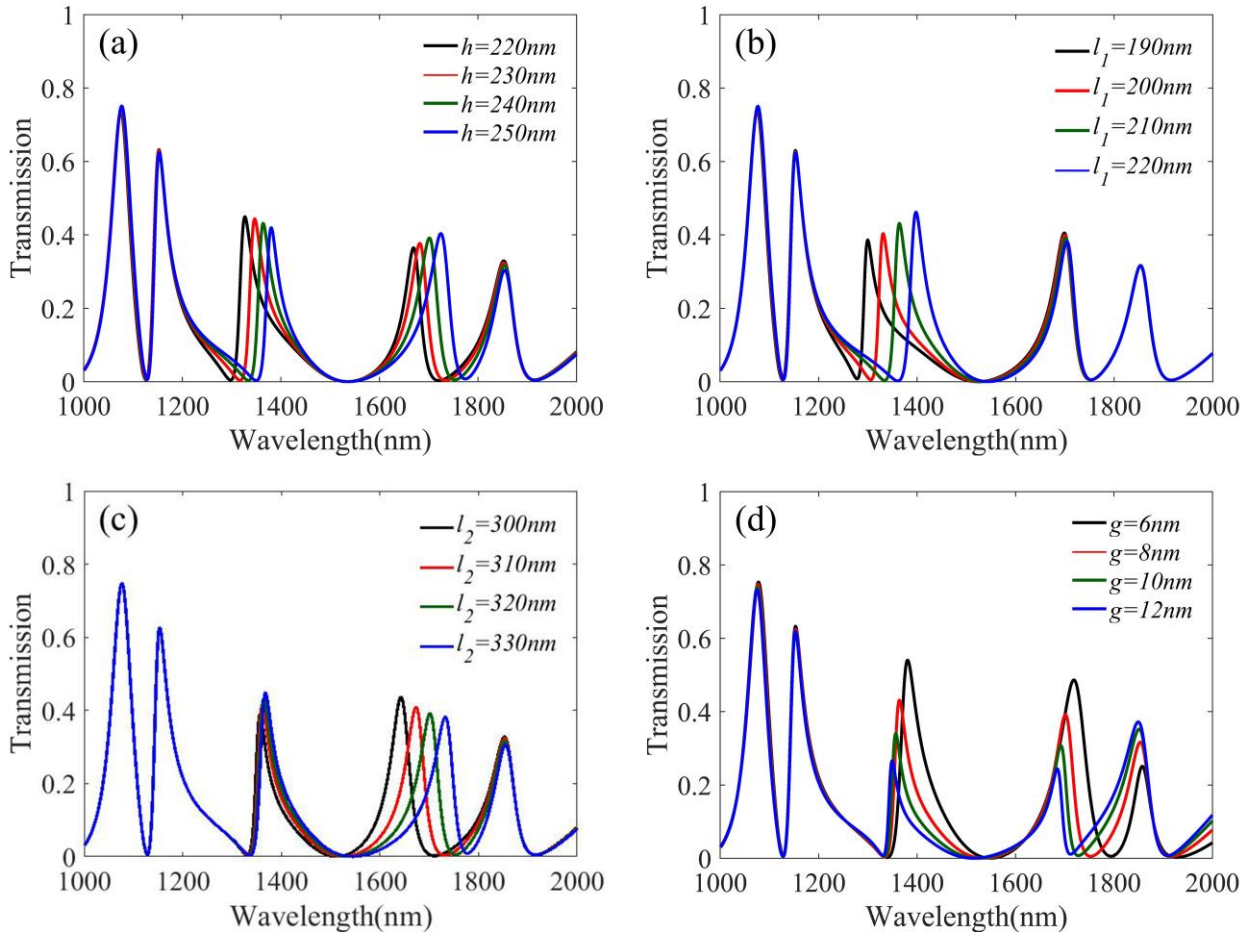

Figure 5 Transmission spectra of different parameters, (a) the height of $cavity1(h_1)$, (b) the left part of the horizontal length(l_1), (c) the right part of the horizontal length(l_2), (d) the coupling distance of $cavity1(g)$.

Then, the influences of adjusting the parameters of $cavity1$ to the transmission spectra are discussed in details. Firstly, the influence of $cavity1$'s height h_1 on

transmission spectrum is studied and the results are shown in Figure 5a.It can be found that $peak2$ and $peak3$ have a significant red-shift when h_1 is increased. The reason is that, increasing h1 results in L_{eff} of these two resonance modes increases, thus increasing the resonance wavelengths of $peak2$ and $peak3$. The results of changing l_1 and l_2 are shown in Figure 5b and c, respectively. Obviously, the length of l_1 affects the position of $peak2$ and the length of l_2 affects the position of $peak3$. All of these results are consistent with Equation 2 and 4, because the changes are corresponding in the effective length L_{eff} of resonator. Then, as shown in Figure 5d, the value of the coupling distance g has a great influence on the transmittance and the FWHM. In the case of g is increased, the decay time τ_n of the coupling between the resonant system and the waveguide will increase, and this can lead both the transmittance and FWHM decreased, which is exactly in agreement with the theoretical analysis of Equation 5-8.

However, the good performance of sensor needs high transmission and narrow FWHM. It's necessary to select the appropriate g to compromise these two parameters. As aforementioned that $peak2$ is controlled by the left and bottom parts of $cavity1$, while the resonance of $peak3$ is produced by the right and bottom parts of $cavity1$. This kind of multiple use of cavity can effectively decrease the size of the structure.

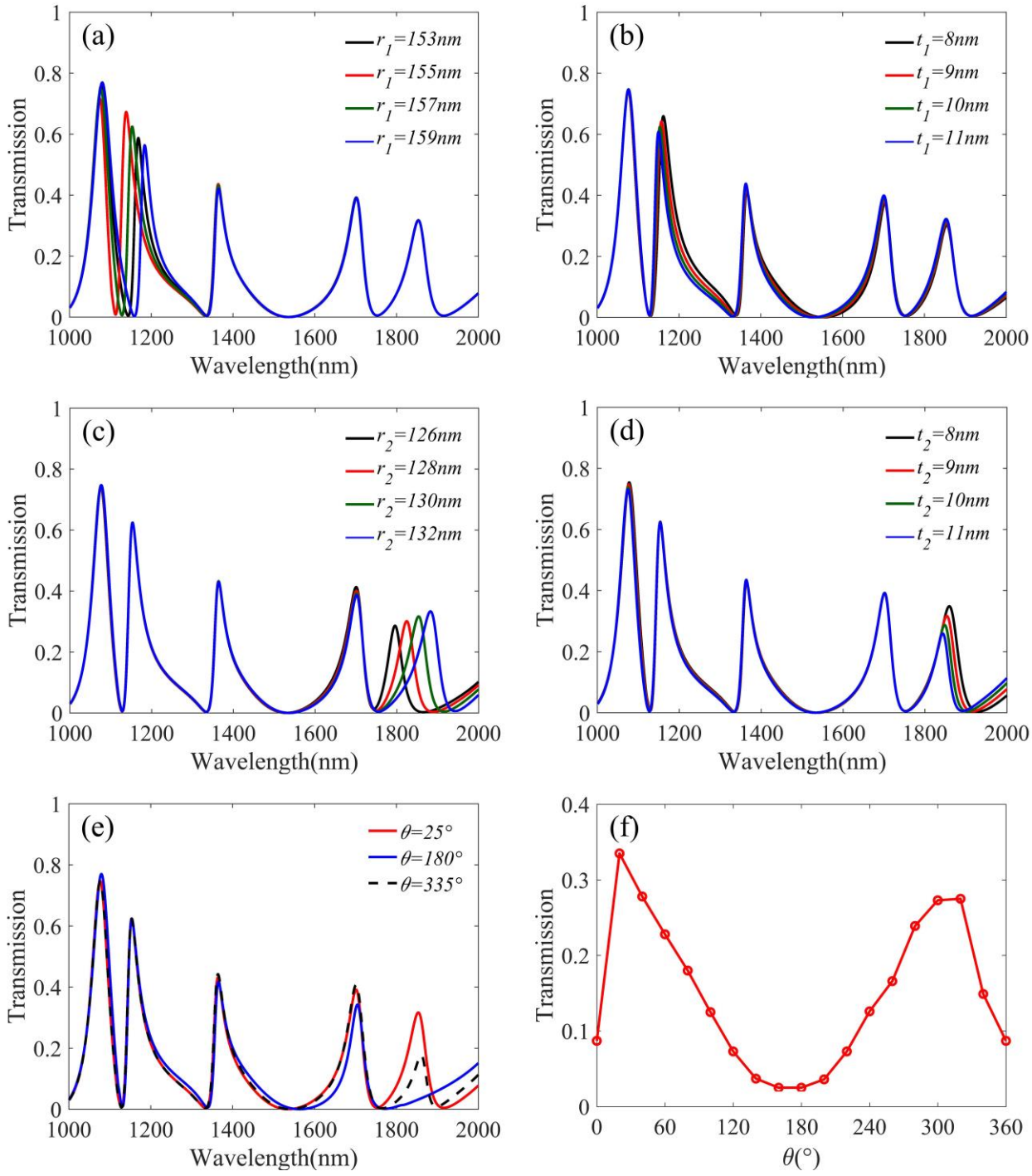

Figure 6 Transmission spectra of (a) the outer radius r_1 of $cavity2$, (b) the coupling distance t_1 of $cavity2$, (c) the outer radius r_2 of $cavity3$, (d) the coupling distance t_2 of $cavity3$ and (e) three specific θ. (f) the dependence of the transmission of $peak5$ on θ.

Subsequently, we investigated the features of $cavity2$ and $cavity3$ on sensing performance. Figure 6a shows the relation between r_1 and the transmission spectra, when the outer radius r_1 of $cavity2$ increases, a significant red shift appears in $peak4$, while the other peaks are stable. A similar situation occurs for the outer radius r_2 of $cavity3$ and $peak5$, as shown in Figure 6c. In Figure 6b and d, we can see that the coupling distance t_1 and t_2 simultaneously affect FWHM, resonance wavelength position and the transmittance of $peak4$ and $peak5$. This is quite similar to the case of the coupling distance g of $cavity1$ discussed above. Therefore, t_1 and t_2 are also not suitable parameters for independent tuning. The tilt angle θ of $cavity3$ also affects the performance of nanosensor. Figure 6e shows the spectra under three special values of θ. Obviously the red and blue lines have five peaks whilst the black dashed line has only four, $peak5$ will disappear when θ is $180°$. In order to further reveal this interesting phenomenon, we simulate the dependence of the transmission on θ and the result is shown in Figure 6f. The peak values of the transmission appear when $\theta = 20°$ and $\theta = 340°(i.e., -20°)$, while the dip values are corresponding to $\theta = 0°$ and $\theta = 180°$.These maximum or minimum values are not rigorous symmetry, which is attributed to the limited height of $stub1$ and its unsymmetrical coupling area with the split-ring, as shown in Figure7.

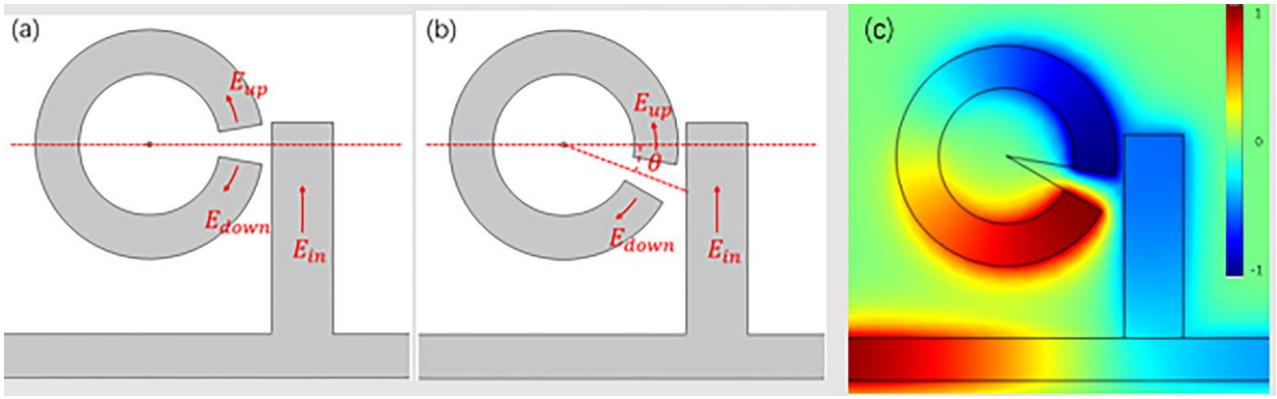

Figure 7 Schematic diagram of $cavity3$ with different tilt angle θ, (a) $\theta = 0°$, (b) $\theta = -20°$. (c) The distribution of magnetic field H_z at $\theta = -20°$.

Afterwards, for the convenience of the following analysis to $cavity3$, the electric field coupled into $cavity3$ is divided into up and down parts named E_{up} and E_{down}, as marked with red arrows along the split-ring in Figure 7. When $\theta = 0°$, as shown in Fig7a, E_{up} and E_{down} are the mirror counterparts, thus produced a typical destructive interference, resulting in a low transmission. The similar phenomenon happens when $\theta = 180°$. When θ is closer to $20°$, the electric field is coupled to one end of $cavity3$, E_{up} almost disappears thus E_{down} dominates the whole coupling process, therefore, a high transmission is generated, which is consistent with the Equation 4. When θ is around $340°$ $(i.e. -20°)$, as shown in Fig7b, one end of $cavity3$ is much closer to $stub1$, thus the corresponding coupled field E_{up} and $E_{down}$of the other end is as shown in Fig7c. This will lead to a slight destructive interference. Compared to the widely used ring resonator, the split-ring almost only takes a quarter of the area to achieve the analogous performance. And the split-ring can be considered as a rectangle rolled up,

which can save space than a conventional rectangular. Besides, the tilt angle θ can be used as a free tuning switch for the structure design.

By analysis above, we can conclude that each resonance mode of our structure has an excellent independence tuning performance.

It is worth mentioning that the sensitivity defined as $S = \Delta\lambda/\Delta n$ and figure of merit(FOM) are important parameters for sensors. Here Δn represents the variation of the refractive index in surrounding environment and $\Delta\lambda$ is the wavelength shift caused by the change of refractive index. The FOM is defined as $FOM = \Delta T/T\Delta n$, where T is the transmission of the structure and $\Delta T/\Delta n$ denotes the transmission change at the fixed wavelength induced by a refractive index change.

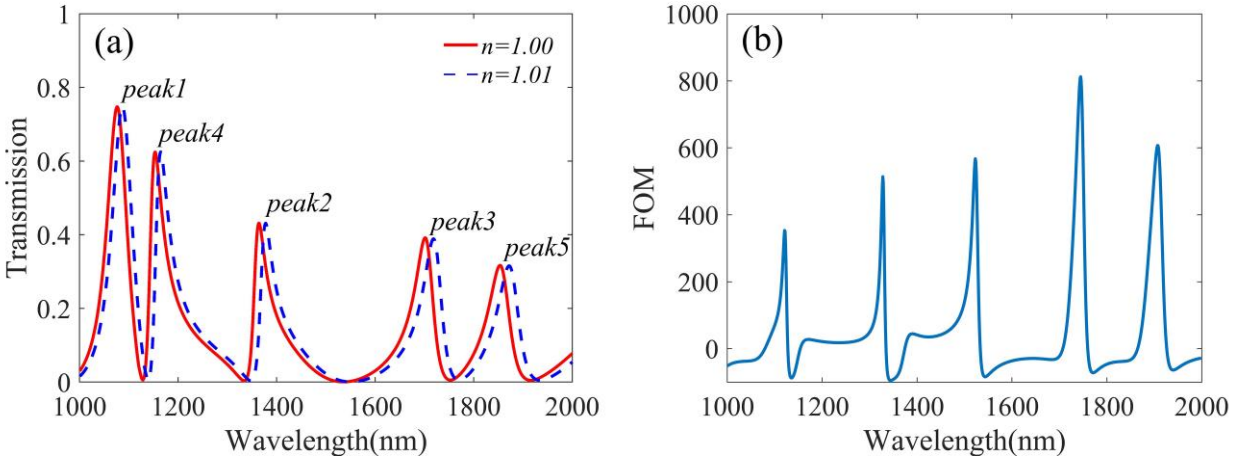

Figure 8 (a) Transmission spectra of different refractive index, (b) the FOM curve of the structure.

Figure 8a shows the transmission spectra when the refractive index of the surrounding environment changes. We can see that a small increase in the refractive index will lead to a significant red shift in the whole spectrum. Then we cal-

culate the sensitivity of each resonance peak, and the results are $1000nm/RIU$, $1400nm/RIU$, $1600nm/RIU$, $1100nm/RIU$ and $1900nm/RIU$ corresponding to $peak1$, $peak2$, $peak3$, $peak4$ and $peak5$, respectively. The step difference of the sensitivity can make the structure have more widely applications. The FOM curve is depicted in Figure 8b. It can be seen that there is a local maximum value of FOM at each dip in the transmission spectrum. The maximum value of the FOM is about 1199 at $1128nm$.

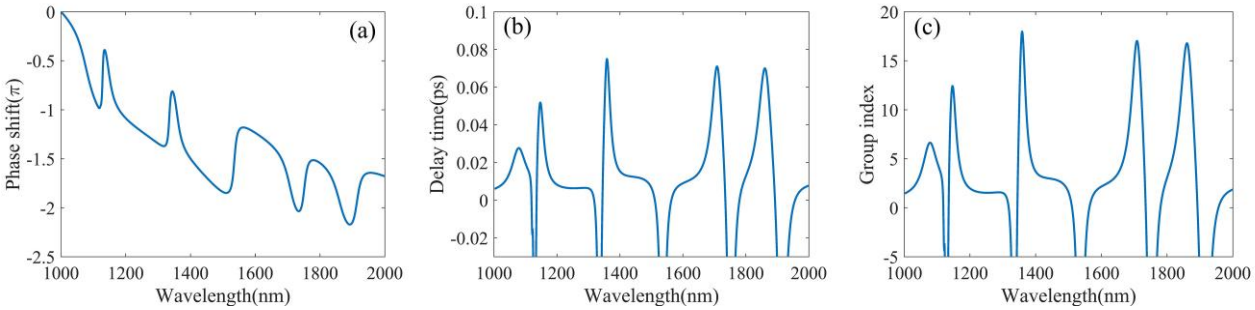

Figure 9 Dependences of (a) phase shift, (b) delay time, (c) group index on the wavelength.

Moreover, the group refractive index of the structure can be calculated by using the phase shift property. Figure 9a shows the phase shift diagram of the structure. From the figure we can see that there is a noteworthy phase shift at each resonance peak. The phase shift can be converted into delay time by $\tau(\lambda) = \mathrm{d}\phi(\omega)/\mathrm{d}\omega$. Then the calculated delay time is shown in Figure 9b. The maximum delay time reaches to $0.075ps$, which leads to the slow light effect. Then the group refractive index and group velocity are calculated by the formula

$$n_g = \frac{c}{v_g} = \frac{c}{D}\tau_g = \frac{c}{D}\frac{\mathrm{d}\phi(\omega)}{\mathrm{d}\omega} \qquad (9)$$

where n_g is the group refractive index, v_g is the group velocity, c represents the speed of light in the free space and D is the distance between the input port and

the output port. Figure 9c shows the dependence between group refractive index and the incident wavelength. It can be seen that the group refractive index is up to 18 at $1359nm$ which is much higher than similar devices and this result is due to its compact size. And at the dip of transmission spectra also can produce fast light effect due to the presence of anomalous group velocity dispersion. Based on Figure 8a and Figure 9c, it can be concluded that the group refractive index obtained at $peak2$ is 16, and its transmission can also reach 0.43, which is an excellent performance for slow light device. Thus, the structure proposed in this paper can also provide a theoretical basis for the slow light structure design in the field of nano-integrated photonic device.

Conclusion

In summary, we report a novel nanosensor which is composed of two stubs and three resonators coupled with MDM waveguide. The results obtained by FEM show that the structure produces five sharp Fano resonances, each of them can easily tuned by changing the specific parameters. After a series of simulation research, we learn that the coupling distance between different cavities needs to be optimized and the structural size parameters are more conducive to free tuning the position of the resonance modes. The multiple cavities, the use of asymmetric structures and a legitimately combination of different resonators make the design dramatically reduce the structure dimensions without sacrificing performance. Furthermore, the plasmonic nanosensor has the maximum of the sensitivity up to $1900nm/RIU$. Compared with similar devices, the more compact size and greater independence are the most outstanding advantages of the structure. The analysis of asymmetric structures in this paper will provide

a powerful theoretical guidance for future plasmonic device design. And our structure may have important potential applications in the compact on-chip plasmonic nanosensors, slow-light devices, spectral splitters, switches, nonlinear photonic devices, etc.

Acknowledgements

This work was supported by the National Natural Science Foundation of China (No. 61804071), the Natural Science Foundation of Gansu Province (Nos. 1606RJZA068 and 18JR3RA297), and the Fundamental Research Funds for the Central Universities of China (lzujbky-2018-129 and lzujbky- 2018-127).

References:

1. Barnes, W. L.; Dereux, A.; Ebbesen, T. W. *NATURE* **2003**, *424*, 824-830.
2. Yang, J.; Song, X.; Chen, Z.; Cui, L.; Yang, S.; Yu, L. *Plasmonics* **2017**, *12*, 1665-1672.
3. Qi, J.; Chen, Z.; Chen, J.; Li, Y.; Qiang, W.; Xu, J.; Sun, Q. *OPTICS EXPRESS* **2014**, *22*, 14688-14695.
4. Zhang, Q.; Huang, X. G.; Lin, X. S.; Tao, J.; Jin, X. P. *Opt Express* **2009**, *17*, 7533-9.
5. Luk Yanchuk, B. S.; Miroshnichenko, A. E.; Kivshar, Y. S. *Journal of Optics* **2013**, *15*, 73001.
6. Chen, Z.; Qi, J.; Chen, J.; Li, Y.; Hao, Z.; Lu, W.; Xu, J.; Sun, Q. *CHINESE PHYSICS LETTERS* **2013**, *30*.
7. FANO, U. *PHYSICAL REVIEW* **1961**, *124*.
8. Li, S.; Zhang, Y.; Song, X.; Wang, Y.; Yu, L. *Optics Express* **2016**, *24*, 15351.
9. Jankovic, N.; Cselyuszka, N. *Sensors* **2018**, *18*, 287.
10. Lu, H.; Liu, X.; Mao, D.; Wang, G. *Optics letters* **2012**, *37*, 3780.
11. Chen, J.; Li, Z.; Zou, Y.; Deng, Z.; Xiao, J.; Gong, Q. *Plasmonics* **2013**, *8*, 1627-1631.
12. Wen, K.; Hu, Y.; Chen, L.; Zhou, J.; Lei, L.; Meng, Z. *Plasmonics* **2016**, *11*, 315-321.
13. Wang, Y.; Li, S.; Zhang, Y.; Yu, L. *Plasmonics* **2018**, *13*, 107-113.
14. Chen, Z.; Song, X.; Jiao, R.; Duan, G.; Wang, L.; Yu, L. *IEEE Photonics Journal* **2015**, *7*, 1-8.
15. Zhao, T.; Yu, S. *Plasmonics* **2018**, *13*, 1115-1120.
16. Zhao, X.; Zhang, Z.; Yan, S. *Sensors* **2017**, *17*, 1494.
17. Wen, K.; Chen, L.; Zhou, J.; Lei, L.; Fang, Y. *Sensors* **2018**, *18*, 3181.
18. Lu, F.; Wang, Z.; Li, K.; Xu, A. *IEEE Transactions on Nanotechnology* **2013**, *12*, 1185-1190.
19. Kun, R.; Xiaobin, R.; Yumeng, H.; Qun, H. *Beilstein Journal of Nanotechnology* **2019**, *10*, 247-255.
20. Wu, C.; Ding, H.; Huang, T.; Wu, X.; Chen, B.; Ren, K.; Fu, S. *Plasmonics* **2018**, *13*, 251-257.
21. Chen, Z.; Yu, L.; Wang, L.; Duan, G.; Zhao, Y.; Xiao, J. *IEEE Photonics Technology Letters*

2015, *27*, 1695-1698.
22. Yun, B.; Zhang, R.; Hu, G.; Cui, Y. *PLASMONICS* **2016**, *11*, 1157-1162.
23. Shi, X.; Ma, L.; Zhang, Z.; Tang, Y.; Zhang, Y.; Han, J.; Sun, Y. *Optics Communications* **2018**, *427*, 326-330.
24. Guo, Z.; Wen, K.; Hu, Q.; Lai, W.; Lin, J.; Fang, Y. *Sensors* **2018**, *18*, 1348.
25. Han, Z.; Bozhevolnyi, S. I. *Optics express* **2011**, *19*, 3251
.
26. Gordon, R. *Physical Review B* **2006**, *73*.
27. White, J. S.; Veronis, G.; Yu, Z.; Barnard, E. S.; Chandran, A.; Fan, S.; Brongersma, M. L. *Opt Lett* **2009**, *34*, 686-8.